Journal of Computational Physics **154,** 372–392 (1999)
Article ID jcph.1999.6319, available online at http://www.idealibrary.com on IDEAL®

Computer Aided Analysis of Viscous Film Flow along an Inclined Wavy Wall

N. A. Malamataris[1] and V. Bontozoglou

Department of Mechanical and Industrial Engineering, University of Thessaly, GR-38334 Volos, Greece

Received December 7, 1998; revised June 15, 1999

The steady, laminar flow of a Newtonian liquid along an inclined wavy wall is studied in a two-dimensional numerical experiment using the Galerkin finite element method. The dimensionless Navier–Stokes equations are solved in the whole range of the laminar flow regime. Numerical predictions are compared with available experimental data for very low Reynolds numbers. The emphasis in the discussion of results is given in the presentation of free surface profiles, streamlines, velocity, and pressure distributions along the free surface and the wall. The interaction of the dimensionless numbers of the flow is studied, criteria for flow reversal are established, and a resonance phenomenon at high Reynolds numbers is investigated.

Key Words: viscous film flow; free surface calculation; finite element method.

1. INTRODUCTION

The flow of a viscous liquid film along a wavy inclined wall is a fundamental fluid mechanics problem. Applications of this flow range from the most common case of heat and mass transfer in heat exchangers and ordered packings [2, 3] up to more advanced technological processes such as electrochemical plating, chemical etching, and chemical conversion in liquid–gas catalytic reactions [4].

Despite the intriguing scientific interest in this problem and the usefulness of its solution, this flow is still not well understood in the whole range of laminar flow both in theory and experiment [2–5]. It is a complex non-linear flow due to the presence of the wavy wall, the free surface, and the influence of inertial and capillary forces.

The simultaneous appearence of these non-linearities render its theoretical solution impossible without the aid of computer aided numerical methods. So far the most thorough solution to this problem in the limit situation of negligible inertial forces has been given by Pozrikidis [4] using the boundary integral method applicable to Stokes flow. Other

[1] To whom correspondence should be addressed at Verias 96, GR-57008 Ionia, Greece. E-mail: nikolaos@eng.auth.gr.

0021-9991/99 $30.00

theoretical solutions to this problem by Wang [6], Dassori *et al.* [7], and Shetty and Cerro [2] use asymptotic methods limited to Stokes flow. There is a need though to study the flow further due to the existence of new results [8] and of theoretical calculations of a resonance phenomenon at high Reynolds numbers by Bontozoglou and Papapolymerou [3].

To the best of our knowledge, there are only two instances of experimental results pertinent to the present problem by Shetty and Cerro [2] and Zhao and Cerro [5]. Cerro and co-workers study the flow of highly viscous liquids along vertical periodic surfaces of five different geometries, where some abovementioned non-linearities influence the flow phenomena. Their data cover a range of very low Reynolds numbers and describe the free-surface topology at steady state.

A resonant interaction between an inclined periodic wavy wall and the free surface has been theoretically predicted by Bontozoglou and Papapolymerou [3] in the limit of sinusoidal wall corrugations of diminishing amplitude. This linear analysis leads to a free surface configuration with the same wavelength as the wall but different amplitude and phase. The most interesting behavior appears for configurations with length around 2 mm. Significant amplification of wall corrugations is calculated for *Re* in the range 150–200 while a 180 degree jump in the phase shift indicates resonant interaction.

The present work has been motivated by the need to give a complete understanding to this problem from a numerical point of view. The Galerkin finite element method is used that enables the tackling of all non-linearities of the problem, as shown by Malamataris and Papanastasiou [9] and Malamataris [10]. In these works, numerical results on non-linear stability analysis, leveling rates of Newtonian fluids [9], and steady state film flow [10, Chap. 5] along a perfectly plane vertical wall compare well with experimental data. The published computer code of these works [10, Appendix C] is now supplemented with boundary conditions involving a spatially periodic wall of arbitrary shape. The flow has been computed as a numerical experiment in a flow field, closely resembling the set-up of an actual laboratory experiment. Thus a realistic entrance section is included. A bonus of this approach—contrasted to imposing infinitely periodic boundary conditions—is additional information on spatial development and the attainment to fully developed flow.

Three different tasks are performed in the present work. First, free surface shapes and streamline patterns are computed for low *Re*-flows for which experimental results are available. The observed agreement validates our numerical procedure. Second, detailed velocity and pressure fields are calculated for flow conditions corresponding to the above experimental data. This information is not available experimentally and serves to improve our understanding for the flow. Third, flow characteristics (and, in particular, free-surface shapes) are calculated at higher Reynolds numbers. In particular, the free-surface/wall resonance [3] theoretically predicted for infinitely small corrugations is recovered and is extended for non-linear wall corrugations.

In the next sections, the problem statement is described along with the governing equations for laminar flow and the appropriate boundary conditions (Section 2). The numerical method is then briefly explained (Section 3), the numerical predictions are presented, discussed, and compared with available experimental data (Section 4), and finally conclusions are drawn (Section 5).

2. GOVERNING EQUATIONS AND BOUNDARY CONDITIONS

The computational domain for the viscous film flow along an inclined wavy wall is shown in Fig. 1. A Newtonian fluid of constant density and viscosity flows in a slit and

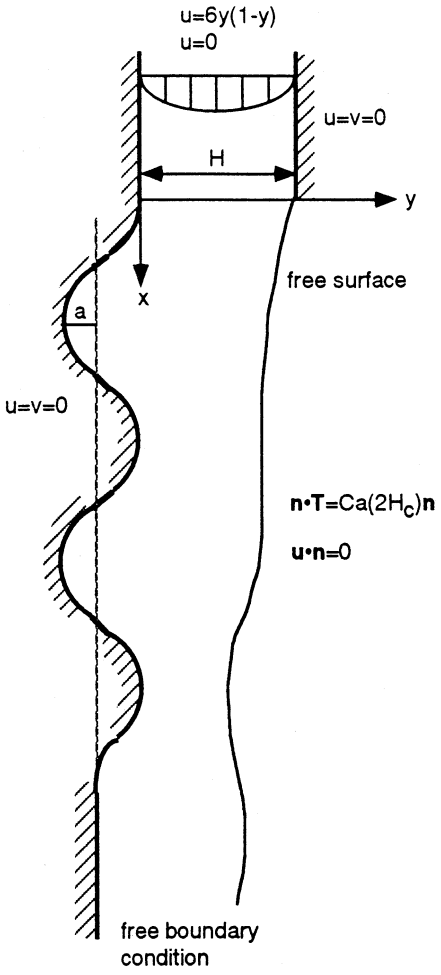

FIG. 1. Computational domain of viscous film flow along an inclined wavy wall.

exits into the ambient air flowing along an inclined wavy wall. Depending on the geometry of the wall, the flow rate, and the properties of the fluid, different free surface shapes are formed and the flow phenomena vary. A complete description of the flow is given by the Navier–Stokes equations along with a kinematic equation of no-mass penetration across the free surface (see Eq. (11)). The flow is laminar, isothermal, incompressible, and two-dimensional. Steady state is considered as a first step in the analysis of this problem and the dimensionless governing equations are

$$\nabla \cdot \mathbf{u} = 0 \tag{1}$$

$$\mathbf{u} \cdot \nabla \mathbf{u} = -\nabla p + \frac{1}{Re}\nabla^2 \mathbf{u} + \frac{1}{Fr}\mathbf{g}. \tag{2}$$

Equations (1) and (2) represent the conservation of mass (continuity equation) and momentum, respectively. Here $\mathbf{u} = (u, v)$ is the dimensionless velocity vector in the fluid, with u and v its components in the x- and y-direction, respectively, and $\mathbf{g} = (\mathbf{i}\sin\alpha, -\mathbf{j}\cos\alpha)$ is the unit vector in the direction of gravity with $\mathbf{i}$ and $\mathbf{j}$ the unit vectors in the x- and y-direction, respectively. Term p is the dimensionless pressure, $Re = \rho Q/\mu$ the Reynolds

number with Q the flow rate per unit span, ρ the density and μ the viscosity of the fluid, and $Fr = U^2/gH$ is the Froude number, with g the magnitude of gravity, H the height of the slit, and $U = Q/H$ the mean velocity of the flow. The pressure p has been nondimensionalized with the magnitude ρU^2. Due to the nondimensionalization of the equations with the flow rate Q and the height of the channel H the Froude number Fr is coupled with the Reynolds number Re,

$$Fr = \frac{Re}{3}\gamma^3 \sin\alpha.$$

Term γ is the dimensionless Nusselt film-thickness [5] given by

$$\gamma = \frac{1}{H}\left(\frac{3\mu Q}{\rho g \sin\alpha}\right)^{\frac{1}{3}}. \tag{3}$$

The boundary conditions for this flow are:

at the entrance

$$u = 6y(1-y) \tag{4}$$

$$v = 0 \tag{5}$$

top and bottom boundaries
in the slit

$$u = 0 \tag{6}$$

$$v = 0 \tag{7}$$

along wavy wall

$$u = 0 \tag{8}$$

$$v = 0 \tag{9}$$

along free surface

$$\mathbf{n}\cdot\mathbf{T} = Ca\,2H_c\mathbf{n} \tag{10}$$

$$\mathbf{n}\cdot\mathbf{u} = 0 \tag{11}$$

at the outflow: free boundary condition.

Equations (4) and (5) impose parabolic slit flow at the entrance of the computational domain. The no-slip boundary condition has been imposed along the walls of the domain (Eqs. (6)–(9)). Stress equilibrium is formulated along the free surface with Eq. (10), where $Ca = \sigma/\rho U^2 H$ is the capillary number, with σ the surface tension of the fluid, $2H_c = h_{xx}/(1+h_x^2)^{3/2}$ the mean free surface curvature, and $\mathbf{T} = -p\mathbf{I} + \frac{1}{Re}(\boldsymbol{\nabla}\mathbf{u} + (\boldsymbol{\nabla}\mathbf{u})^T)$ the dimensionless stress tensor of the fluid, with $\mathbf{I}$ the identity matrix. Equation (10) accounts for the effects of surface tension along the free surface of the falling film. Equation (11) is the condition of no-mass penetration across the free surface, which is solved simultanously with the governing equations to yield the location of the free surface at each point of the computational domain. It should be noted that it is not necessary to prescribe an angle of the free surface at the exit of the slit (see Fig. 1), as at that point the location of the free surface

coincides with the slit height, due to the no-slip boundary condition for the velocity vector $\mathbf{u}$ (see Eqs. (6)–(7)). Term $\mathbf{n} = (-h_x\mathbf{i} + \mathbf{j})/\sqrt{1+h_x^2}$ is the unit vector normal to the free surface, with h the location of the free surface and $h_x = \partial h/\partial x$. The flow may be specified by the following independent dimensionless groups: the Reynolds number, *Re*, the capillary number, *Ca*, and the Nusselt film thickness, γ.

The free boundary condition has been applied at the outflow in order to let the fluid leave the computational domain freely without any distortion of the flow in the interior. The next section briefly outlines how this idea [9, 11] is included in the formulation of the finite element method by evaluating the surface integral of Eq. (15). It is beyond the scope of this work to get into the details of its implementation, which can be found elsewhere [10] or into its mathematical insight, which has, to a significant extent, been accomplished by Sani and Gresho [12; 13, p. 103], Heinrich and Vionnet [14], Griffiths [15], and Renardy [16].

3. FINITE ELEMENT FORMULATION

The primary unknowns of the flow, which are the velocities u_i and v_i and the pressure p_i of the Navier–Stokes equations (1), (2) along with the unknown location of the free surface h_i in the kinematic equation (11), are expanded in terms of Galerkin basis functions as

$$u = \sum_{i=1}^{9} u_i\phi^i, \qquad v = \sum_{i=1}^{9} v_i\phi^i, \qquad h = \sum_{i=1}^{9} h_i\phi^i, \qquad p = \sum_{i=1}^{4} p_i\psi^i,$$

where ϕ^i are biquadratic and ψ^i bilinear basis functions. This is a standard choice of basis functions in Gakerkin finite element method analysis of flow problems as discussed in detail by Gresho and Sani [13, p. 459] and Peyret and Taylor [17, p. 218]. The governing equations, weighted integrally with the basis functions, resulted in the following continuity, R_C^i, momentum, R_M^i, and kinematic, R_K^i, residuals:

$$R_C^i = \int_V \boldsymbol{\nabla}\cdot\mathbf{u}\psi^i\, dV \tag{12}$$

$$R_M^i = \int_V \left[\mathbf{u}\cdot\boldsymbol{\nabla}\mathbf{u} - \boldsymbol{\nabla}\cdot\left(-p\mathbf{I} + \frac{1}{Re}(\boldsymbol{\nabla}\mathbf{u} + (\boldsymbol{\nabla}\mathbf{u})^T)\right) + \frac{1}{Fr}\mathbf{g}\right]\phi^i\, dV \tag{13}$$

$$R_K^i = \int_S (h_x u - v)\phi^i|_{\eta=1}\, dS. \tag{14}$$

By applying the divergence theorem, in order to decrease the order of differentiation, Eq. (13) reduces to

$$R_M^i = \int_V \left[\left(\mathbf{u}\cdot\boldsymbol{\nabla}\mathbf{u} + \frac{1}{Fr}\mathbf{g}\right)\phi^i - \left(-p\mathbf{I} + \frac{1}{Re}\mathbf{T}\right)\cdot\boldsymbol{\nabla}\phi^i\right] dV$$
$$- \int_S \mathbf{n}\cdot\left(-p\mathbf{I} + \frac{1}{Re}(\boldsymbol{\nabla}\mathbf{u} + (\boldsymbol{\nabla}\mathbf{u})^T)\right)\phi^i\, dS. \tag{15}$$

Since essential boundary conditions for u and v are applied to all boundaries of the domain except for the outflow and along the free surface, Eq. (15) will be replaced by Eqs. (4)–(9). Along the free surface of the computational domain, the surface integrand of Eq. (15) will be replaced by Eq. (10). A novel point in the implementation is the evaluation of Eq. (15)

along the outflow. Instead of imposing some sort of boundary conditions (e.g., periodic), we extend the range of the Galerkin expansion up to and including the outflow. As a result, the outflow conditions come as part of the solution and it is not necessary to prescribe the angle at the free surface end. This allows description of the developing flow without reflections caused by arbitrary boundary conditions. Details on the programming strategy and the actual implementation of the free boundary condition can be found elsewhere [10].

The residuals are evaluated numerically using nine-point Gaussian integration, which is a good compromise between accuracy and computational efficiency [13, p. 44], as shown by numerical experimentation. A system of non-linear algebraic equations results, which is solved with the Newton–Raphson iterative method according to the scheme $\mathbf{q}^{(n+1)} = \mathbf{q}^{(n)} - \mathbf{J}^{-1}\mathbf{R}(\mathbf{q}^{(n)})$ where $\mathbf{q}^T = [u_1, v_1, p_1, h_1 \ldots, u_N, v_N, p_N, h_N]$ is the vector of the unknowns and $\mathbf{J} = \partial\mathbf{R}/\partial\mathbf{q}$ is the Jacobian matrix of the residuals $\mathbf{R}$ with respect to the nodal unknowns $\mathbf{q}$. The banded matrix of the resulting linear equations is solved with a frontal solver [18] at each iteration. The computer runs have been performed at a DEC OSF/1 V3.2-Alpha 7000-610 AXP. A 0th order continuation has been used as an initial guess to advance from one solution to another and the Newton iteration of all computer runs converged quadratically in 4–6 iterations, independent of the mesh resolution. All numerical results are mesh independent as evidenced by the fact that increased mesh refinement influences the accuracy of the solution less than 10^{-6}.

4. RESULTS AND DISCUSSION

The results of this work are presented in the following way: First numerical experiments have been performed along a vertical wavy wall with an S- and C-shaped geometry, as studied in the work of Zhao and Cerro [5], and under their experimental conditions. Comparison of our results with their experiments encouraged us for further numerical runs at higher Reynolds numbers, enabling the validation of the predictions of Bontozoglou and Papapolymerou [3], which is discussed at the end of this section.

Numerical experiments of viscous film flow along a vertical S-shaped wall. The geometry of the S-shaped vertical wall consists of a combination of two semi-circles of radius 1.5875 mm. We used a computational mesh of 5 periods of S-shaped undulations followed by a flat section of one wavelength. A representative converged mesh is depicted in Fig. 2 for one period of wall undulations and the computational details of the runs are summarized in Table I. The height of the slit is 1 mm, in accordance with the flow distributor of the experimental design of Zhao and Cerro [5, p. 499]. They performed the experiments of this flow configuration using silicon oil, glycerol A and B.

The complete free surface is shown in Fig. 3 for a representative run. Periodicity is attained almost after the first groove. Thus, the caution exercised by Zhao and Cerro, in taking measurements after 10–15 grooves to assure fully developed flow [5, p. 498], seems unnecessary in these numerical experiments. The situation, however, may differ at higher Reynolds numbers. It is also shown that the wavelength of oscillation of the free surface is identical to the wavelength of wall undulations accompanied by a slight phase shift, which has been observed both experimentally [5] and theoretically [4, 6].

Results of free surface shape are shown in Fig. 4 and are compared with the corresponding experimental data of Zhao and Cerro. The agreement is by inspection satisfactory. As the flow rate decreases in Fig. 4a the oscillation of the free surface increases and tends to follow

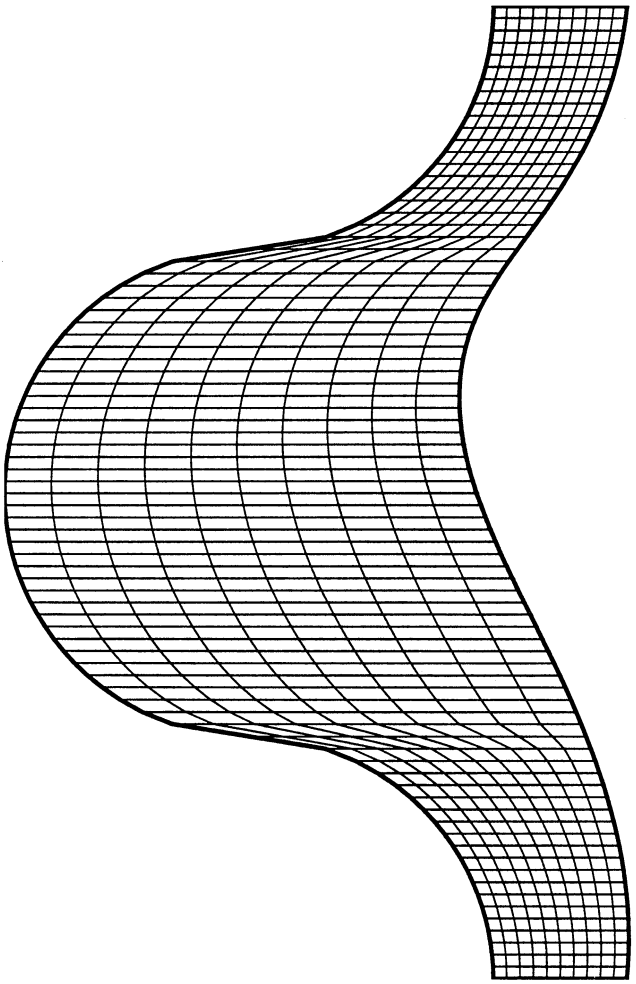

FIG. 2. Converged mesh in the S-set of numerical experiments for one period of wall undulations.

the shape of the wall curvature, as reported also by Pozrikidis [4, p. 284]. However, the action of capillary forces and the high value of the capillary number in the limit of zero flow rate maintain a phase-shift in the periodicity of the free surface and prevent liquid film from exactly following the wavy wall profile.

Increasing surface tension acts to decrease the free surface curvature, as is evident by comparison of Fig. 4a with Figs. 4b and 4c. A side-effect of this behavior is a marked difference in the draining process with decreasing flow rate. Silicon oil (Fig. 4a) drains easily from the grooves forming a film of, more or less, uniform thickness. On the contrary, the higher surface tension of glycerol (Figs. 4b and 4c) leads to retension of fluid pockets at the wall troughs, which persist with diminishing flow rate.

Numerical results for the calculation of the film thickness curve and the free surface curve are compared with the experimental data of Zhao and Cerro in Fig. 5. The agreement is very satisfactory, as is the case in Fig. 6, where streamlines of an actual flow visualization are compared to numerical computations for a representative experiment. We calculated no flow reversal at any magnitude of the flow rate for this set of experiments, in accordance with the experimental observations of Zhao and Cerro [5, p. 507].

TABLE I
Computational Details for the S-Set of Numerical Experiments

Number of elements	4280
Number of nodes	17,997
Number of unknowns	41,570
Number of grooves	5
Matrix front width	62
CPU per iteration	30 s

x-coordinate of the nodes before the grooves

−3., −2.5, −2., −1.5, −1., −0.75, −0.5, −0.4, −0.3, −0.2, −0.1, −0.05, −0.025, 0

x-coordinate of the nodes in the grooves (multiples of the radius of the groove in 1/4th of the period)

0., 0.05, 0.1, 0.15, 0.2, 0.25, 0.3, 0.35, 0.4, 0.45, 0.5, 0.55, 0.6, 0.65, 0.7, 0.75, 0.8, 0.85, 0.9, 0.95, 1

x-coordinate of the nodes after the grooves

31.75, 32., 32.25, 32.5, 32.75, 33., 33.25, 33.5, 33.75, 34., 34.5, 35., 35.5, 36., 36.5, 37

y-coordinate of the nodes (multiples of the height of the free-surface)

0., 0.1, 0.2, 0.3, 0.4, 0.5, 0.6, 0.7, 0.8, 0.9, 1

Since finite element analysis yields a complete picture of the flow field, it is interesting to examine how other magnitudes of the flow vary for this experimental set-up, although there is a lack of corresponding laboratory experimental data. In Figs. 7a and 7b, it is depicted how the x- and y-components of the velocity at the free surface vary along the free surface. As the flow rate decreases, free surface amplitude increases and accordingly variation of the y-component of free surface velocity becomes more distinct in magnitude. The v-velocity reaches its absolute minimum where the free surface is over the point of contact of the two semi-circles and the flow goes into the deep part of the groove. The absolute maximum of the v-velocity is reached where the free surface is over the half of the last semi-circle and fluid leaves the deepest part of the groove.

Variation of the u-velocity as a function of cross-section of the flow is shown in Figs. 7c, 7d for the two extreme flow rates of Fig. 4a. The x-component of free surface velocity reaches its absolute minimum in the deep part of the groove, where—due to mass conservation—the cross section of the flow is maximum. Maximum of the u-component of free surface

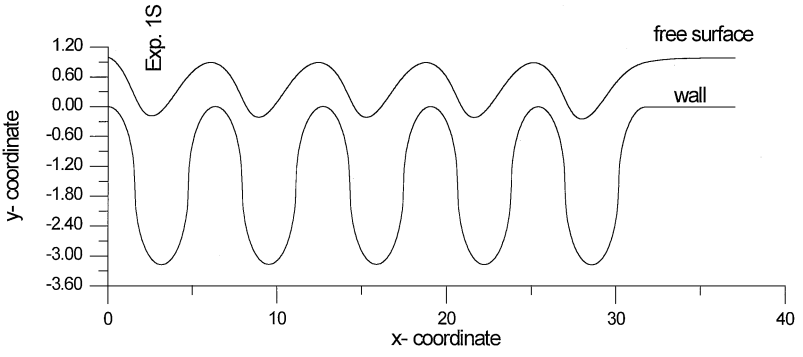

FIG. 3. Display of periodicity in the S-set of numerical experiments. The arrows display the velocity vector.

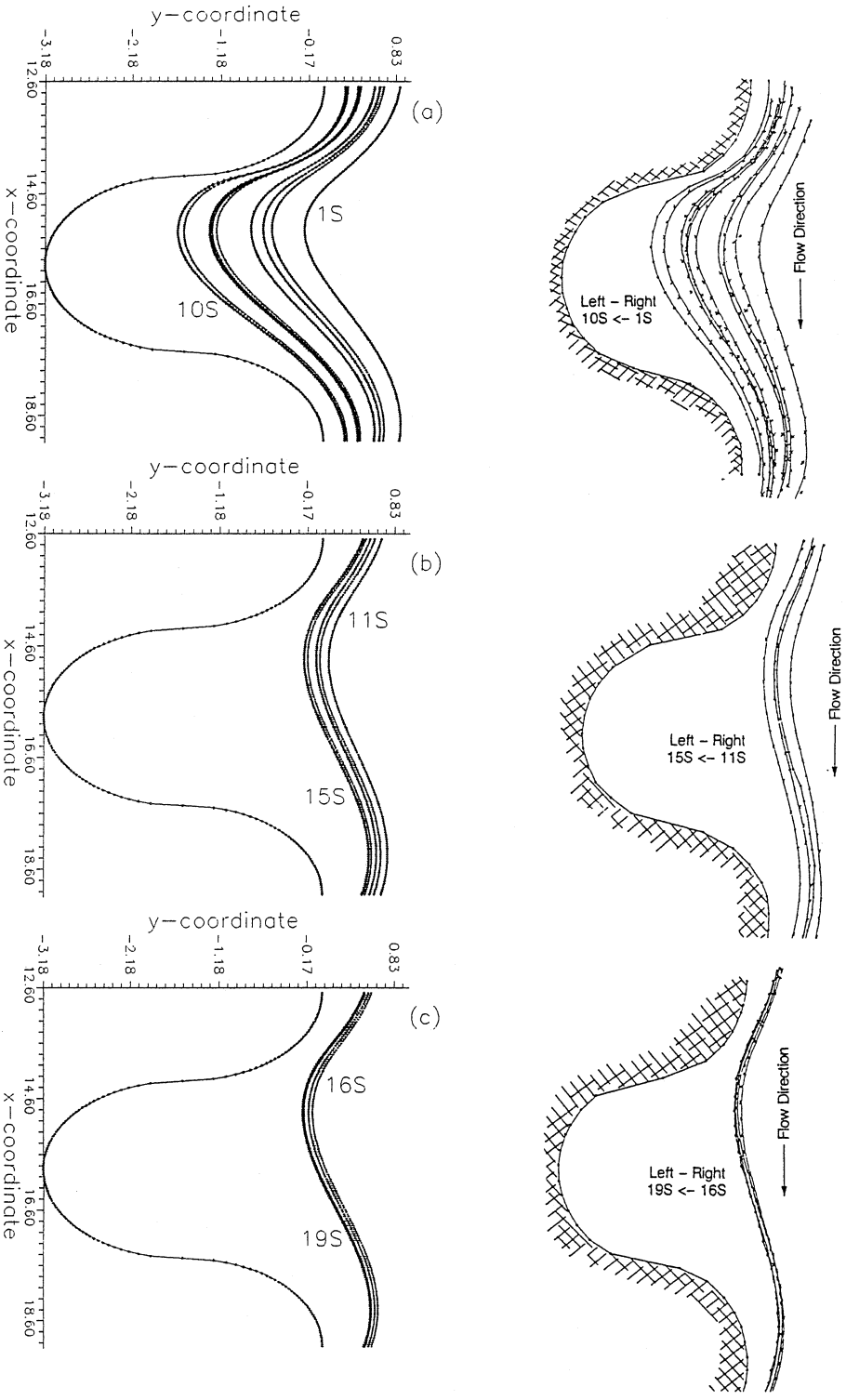

FIG. 4. Comparison of numerical versus laboratory experiments for the periodic free surface profiles of viscous film flow along a vertical S-shaped wall.

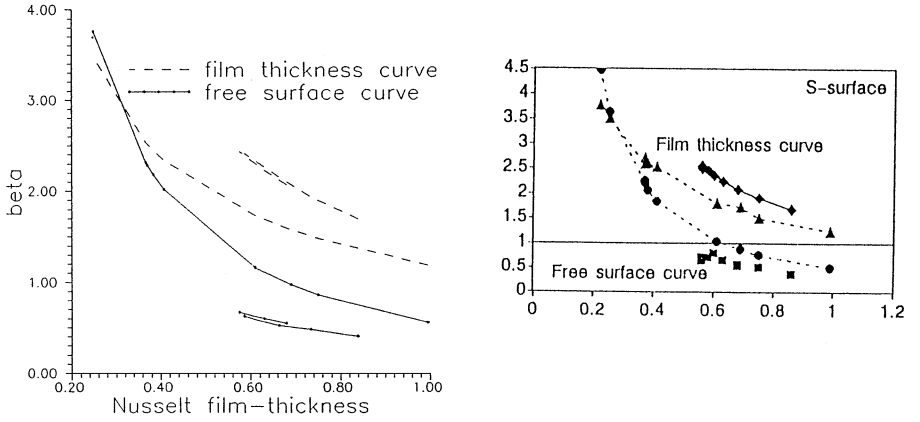

FIG. 5. Comparison of numerical versus laboratory experiments for the calculation of the free surface curve and the film thickness curve of viscous film flow along a vertical S-shaped wall.

velocity is reached at the edges of each period of undulations, following the same reasoning of the law of continuity. As flow rate decreases, a local maximum in the u-velocity emerges, where the free surface is over the point of contact of the two semi-circles, due to the sudden diminuation of flow cross-section at that point (see also Fig. 4). As in the case of the v-component of free surface velocity, the u-component as well exhibits more pronounced variation in magnitude as flow rate decreases and free surface amplitude increases.

Finally, dimensionless mean velocity of the corresponding Nusselt flow [5], given as $u^* = (\rho g L^3/3\mu Q)^{1/3}$, ranges from $1.0048 \leq u^* \leq 4.5$. In all cases, the u component of free

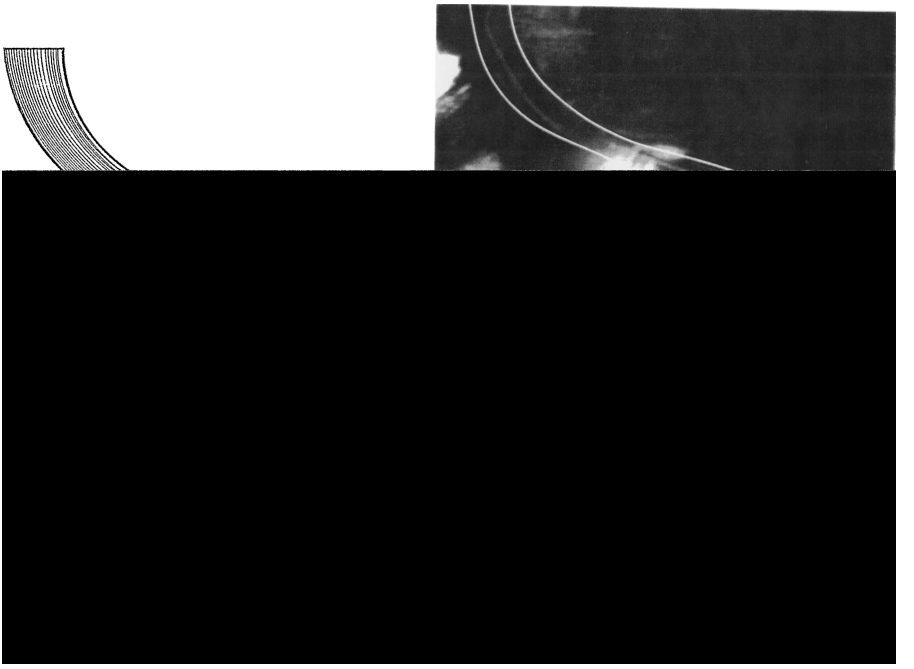

FIG. 6. Comparison of numerical versus laboratory experiment for the streamlines of a representative experiment.

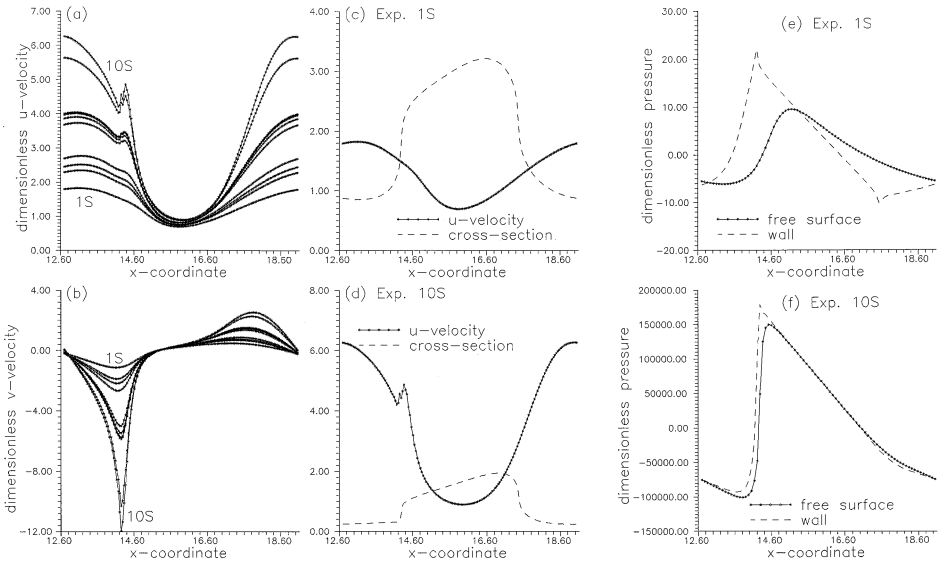

FIG. 7. (a) and (b) Distribution of the u- and v-component of the velocity of the free surface for the viscous film flow along a vertical S-shaped wall. (c) and (d) Variation of the u-velocity as a function of the horizontal cross-section of the film flow in the S-set of numerical experiments. (e) and (f) Distribution of the pressure along the free surface and the wall for the viscous film flow along a vertical S-shaped wall.

surface velocity obtains values considerably higher than u^*, which is in accordance with the experimental observations of Zhao and Cerro [5, p. 508].

Pressure distribution along the free surface and the wall is depicted in Figs. 7e, 7f for the S-set of numerical experiments. In all pressure profiles, the point of absolute maximum of the free surface pressure coincides with the absolute minimum of the velocity magnitude, in accordance with Bernoulli's energy conservation law. Pressure along the wall reaches its absolute maximum in the region of the point of contact of the two semi-circles, where flow goes deep into the groove and the dynamic effect of maximum v-velocity component of the free surface (see Fig. 7b) increases the pressure along the wall. It is noted that if the wall were completely flat there would be no difference in the pressure distribution along the free surface and the wall, since the flow is vertical and there is no hydrostatic pressure effect. The wavy nature of the flow though along with the action of capillary forces cause a departure from that behavior.

Numerical experiments of viscous film flow along a vertical C-shaped wall. The geometry of the C-shaped wall consists of a sequence of semi-circles of radius 1.5875 mm separated by a 0.2 mm flat section. For this series of experiments, Zhao and Cero [5] used a mixture of water–glycerin 1 : 2, silicon oil, and glycerol-B. Nine periods of wall undulations have been chosen for this set of numerical experiments, in order to achieve periodicity of the free surface profile. This length of computational domain is comparable to five periods of the previous set of numerical experiments (see Fig. 3), since the period of undulations of the S-shaped wall is twice as long. A representative converged mesh is depicted in Fig. 8 for one period of wall undulations and the computational details of the runs are summarized in Table II. Periodicity of the numerical experiments of this set is demonstrated in Fig. 9, where free surface shape of a representative numerical experiment is shown in the whole computational domain. Again, the wavelength of oscillation coincides with the wavelength

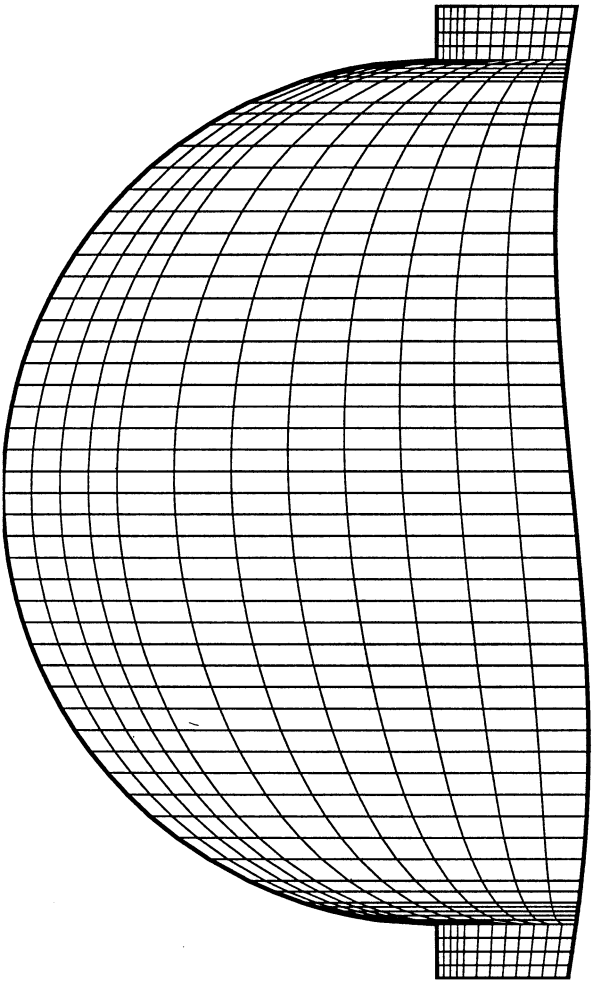

FIG. 8. Converged mesh in the C-set of numerical experiments for one period of wall undulations.

of wall undulations and the phase difference is due to the action of inertial and capillary forces, as already discussed in the previous set of numerical experiments.

Free surface profiles are again in agreement with the laboratory experiments, as shown in Fig. 10 and analogous agreement is also found in the comparison of the film thickness curve and free surface curve (Fig. 11). The oscillations of the free surface profiles of the C-set of experiments is appreciably less than in the S-set although flow parameters are of the same order of magnitude. This is attributed to the different geometry of the C-shaped wall, which has a shallower groove and due to the wavelength of the undulation, which is half the wavelength of the S-shaped wall.

An interesting new feature concerns the formation of a recirculation region (stagnation pocket) for the experiments of Fig. 10a (see Fig. 12), which correspond to the highest flow rates, as also observed by Zhao and Cerro [5, p. 508]. The strange patterns around the corners of Fig. 12 represent small recirculations, that are not adequately described, because of the highly distorted finite element mesh at that region as shown in Fig. 8. However, the effect is local and in no way affects the convergence and accuracy of the solution. A well known fact for recirculation zones [4, 21, 22] is the change of sign in the shear stress distribution

TABLE II
Computational Details for the C-Set of Numerical Experiments

Number of elements	6072
Number of nodes	25,325
Number of unknowns	58,254
Matrix front width	72
CPU per iteration	50 s

x-coordinate of the nodes before the grooves

−3., −2.5, −2., −1.5, −1., −0.75, −0.5, −0.4, −0.3, −0.2, −0.1, −0.05, −0.025, 0

x-coordinate of the nodes in the grooves (multiples of the radius in the groove)

0., 0.01, 0.02, 0.03, 0.04, 0.05, 0.1, 0.125, 0.15, 0.2, 0.25, 0.3, 0.35, 0.4, 0.45, 0.5, 0.55, 0.6, 0.65, 0.7, 0.75, 0.8, 0.85, 0.9, 0.95, 1., 1.05, 1.1, 1.15, 1.2, 1.25, 1.3, 1.35, 1.4, 1.45, 1.5, 1.55, 1.6, 1.65, 1.7, 1.75, 1.8, 1.85, 1.9, 1.925, 1.95, 1.96, 1.97, 1.98, 1.99, 2

x-coordinate of the nodes in the flat section of the first groove

3.175, 3.225, 3.275, 3.325, 3.375

x-coordinate of the nodes after the grooves

30.375, 30.5, 30.75, 31., 31.25, 31.5, 31.75, 32

y-coordinate of the nodes (multiples of the height of the free-surface)

0., 0.05, 0.1, 0.15, 0.2, 0.3, 0.4, 0.5, 0.6, 0.7, 0.8, 0.9, 1

along the wall, where reattachment of the flow occurs. For these runs, the distribution of shear stress and vorticity has been calculated and shown in Fig. 13. Both shear stress and vorticity change sign almost at the point of reattachment of the flow. At all lower flow rates no flow reversal was computed, in agreement with the experimental observations of Zhao and Cerro.

There is some arguing as to how the recirculation region is generated. Zhao and Cerro state that it is the value of the flow rate, while Pozrikidis [4, p. 290] adds that, apart from a critical value in the flow rate, flow reversal also occurs with increasing film thickness. In order to clarify this phenomenon, we performed numerical experiments at the flow conditions of the run of Fig. 10b, by changing only one dimensionless parameter at a time. Results for the streamlines are shown in Fig. 14. In all three cases (Fig. 14b, $Ca = 1$; Fig. 14c,

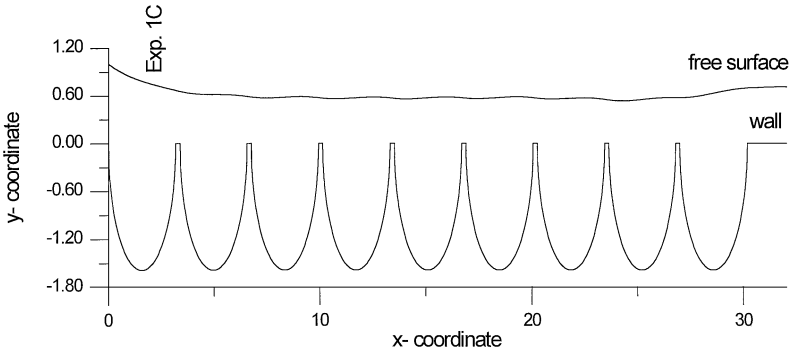

FIG. 9. Display of periodicity in the C-set of numerical experiments. The arrows display the velocity vector.

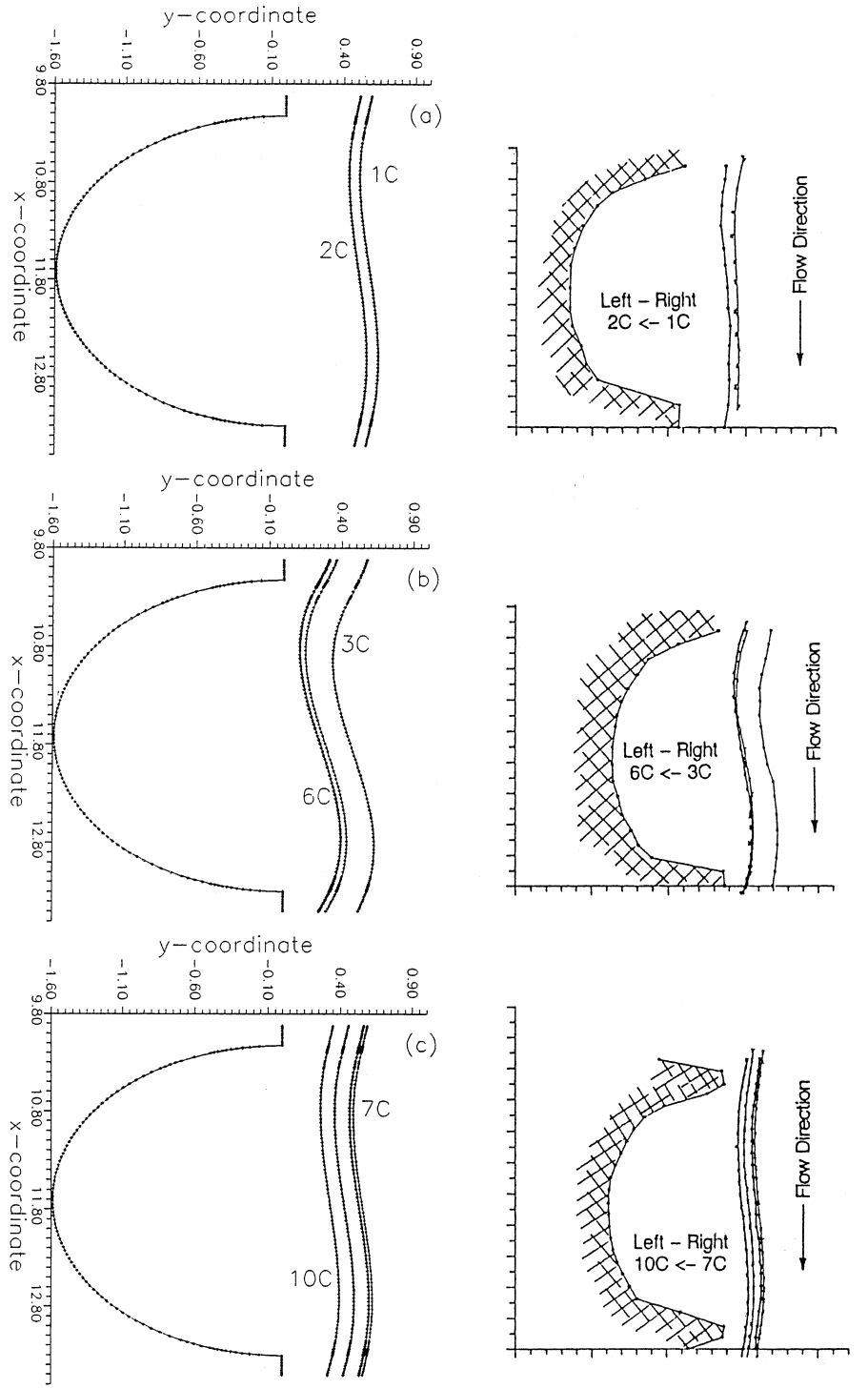

FIG. 10. Comparison of numerical versus laboratory experiments for the periodic free surface profiles of viscous film flow along a vertical C-shaped wall.

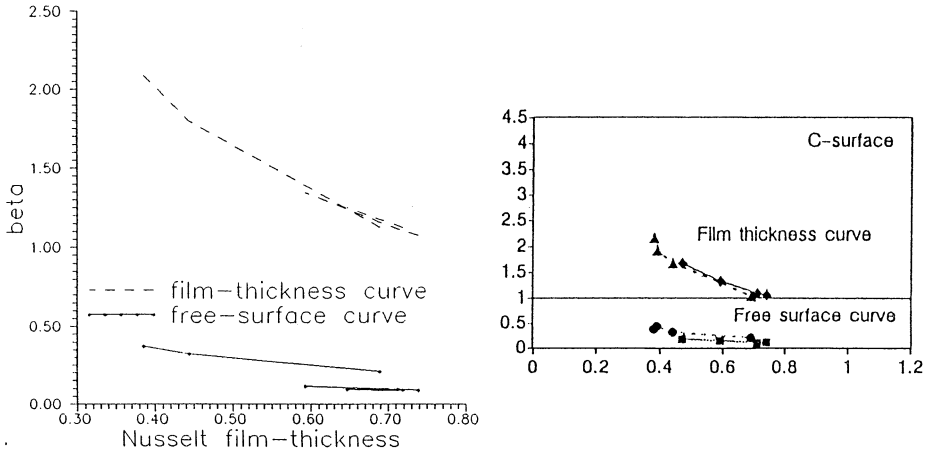

FIG. 11. Comparison of numerical versus laboratory experiments for the calculation of the free surface curve and the film thickness curve of viscous film flow along a vertical C-shaped wall.

$\gamma = 0.4$; Fig. 14d, $Re = 1.5$) the recirculation zone disappears. A common characteristic in all these runs is the supression of flow reversal, due to decreasing film thickness. Indeed, the arguments of Zhao, Cerro, and Pozrikidis are verified, as a decrease in the flow rate and the dimensionless Nusselt film thickness inhibits flow reversal. However, an additional cause of inhibition of flow recirculation is the decrease of surface tension. Apart from this new finding, Fig. 14 displays the different influence of each dimensionless number in the flow: Reynolds number influences the phase shift of the free surface, capillary number affects its shape, and dimensionless Nusselt film thickness reduces its thickness. Finally, velocity and pressure distributions for these runs follow the same pattern as in the previous set of experiments and are not presented.

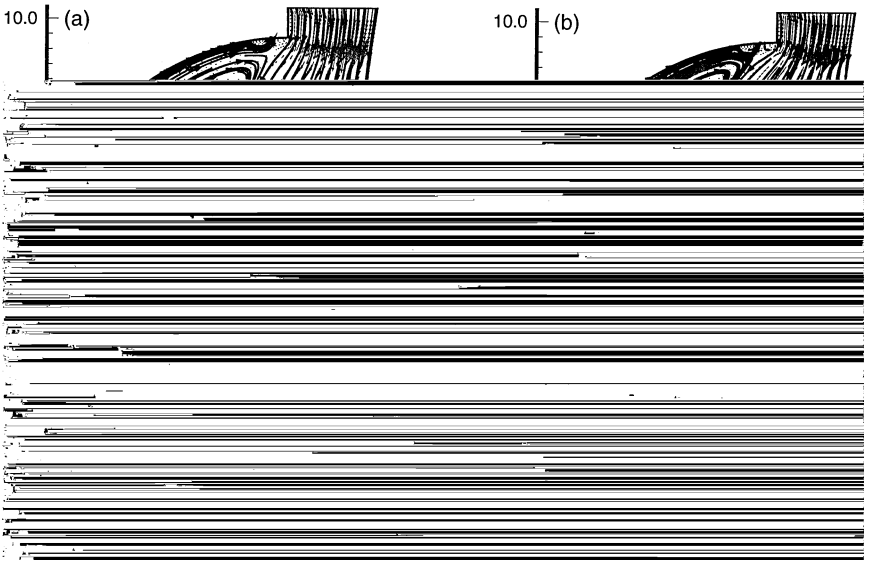

FIG. 12. Calculated streamlines for numerical experiments of the highest flow rates of the C-set of experiments. The arrows display the velocity vector.

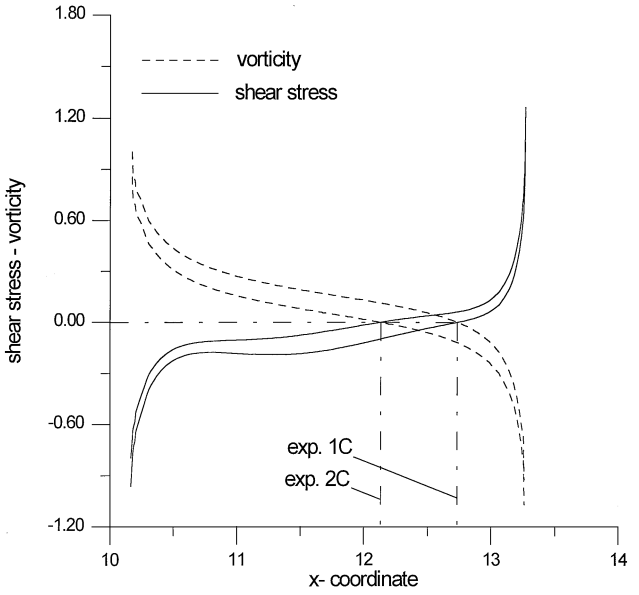

FIG. 13. Distribution of shear stress and vorticity for numerical experiments of Fig. 12.

Numerical experiments of viscous film flow along an inclined sinusoidally shaped wall at high Reynolds numbers. The satisfactory agreement of numerical experiments with existing laboratory data, which yield a complete picture of the flow phenomena supplementing the laboratory experiments, encourages application of the computer code of this work to higher Reynolds numbers. The goal is to validate and extend recent linear theoretical results by Bontozoglou and Papapolymerou [3], who have predicted a resonance phenomenon at the free surface for water flow along an inclined wall with sinusoidal infinitesimal indentations of length L around 2 mm.

Numerical experiments have been carried out in the whole range of laminar flow and in Fig. 15 results are shown for the case of infinitesimal wall undulations ($a = 0.01$). Up to $Re = 50$ the free surface is almost a straight line without any appreciable oscillations. As the Reynolds number increases the oscillations increase and around $Re = 180$ we observe the predicted resonance [3]. Maximum amplification of the oscillation at the free surface is roughly equal to twice the oscillation of the wall, in agreement with the linear limit calculated by Bontozoglou and Papapolymerou [3]. At even higher Reynolds numbers, free surface oscillations are shifted closer to the entrance with diminishing amplitude until they gradually fade at $Re = 400$. Free surface resonance is prevented at $Re \ll 180$ by high value of capillary number and at $Re \gg 210$, by the high value of dimensionless Nusselt film thickness.

In Figs. 16–17, it is shown how the oscillations of the free surface change for wall indendations of finite amplitude ($a = 0.1$). In this case oscillations in the region $180 \leq Re \leq 210$ are intensified and maximum amplitude of free surface oscillations is 1.5 times higher than wall amplitude. At Reynolds numbers outside this "resonant" region, free surface oscillations are also enhanced, in the same fashion though as in the case of infinitesimal wall undulations.

Two interesting non-linear phenomena are observed for the non-linear case: Maximum amplification occurs around $Re = 210$. It, thus, seems that there is a shift of resonance to higher Reynolds numbers with increasing wall amplitude. The dominant free-surface

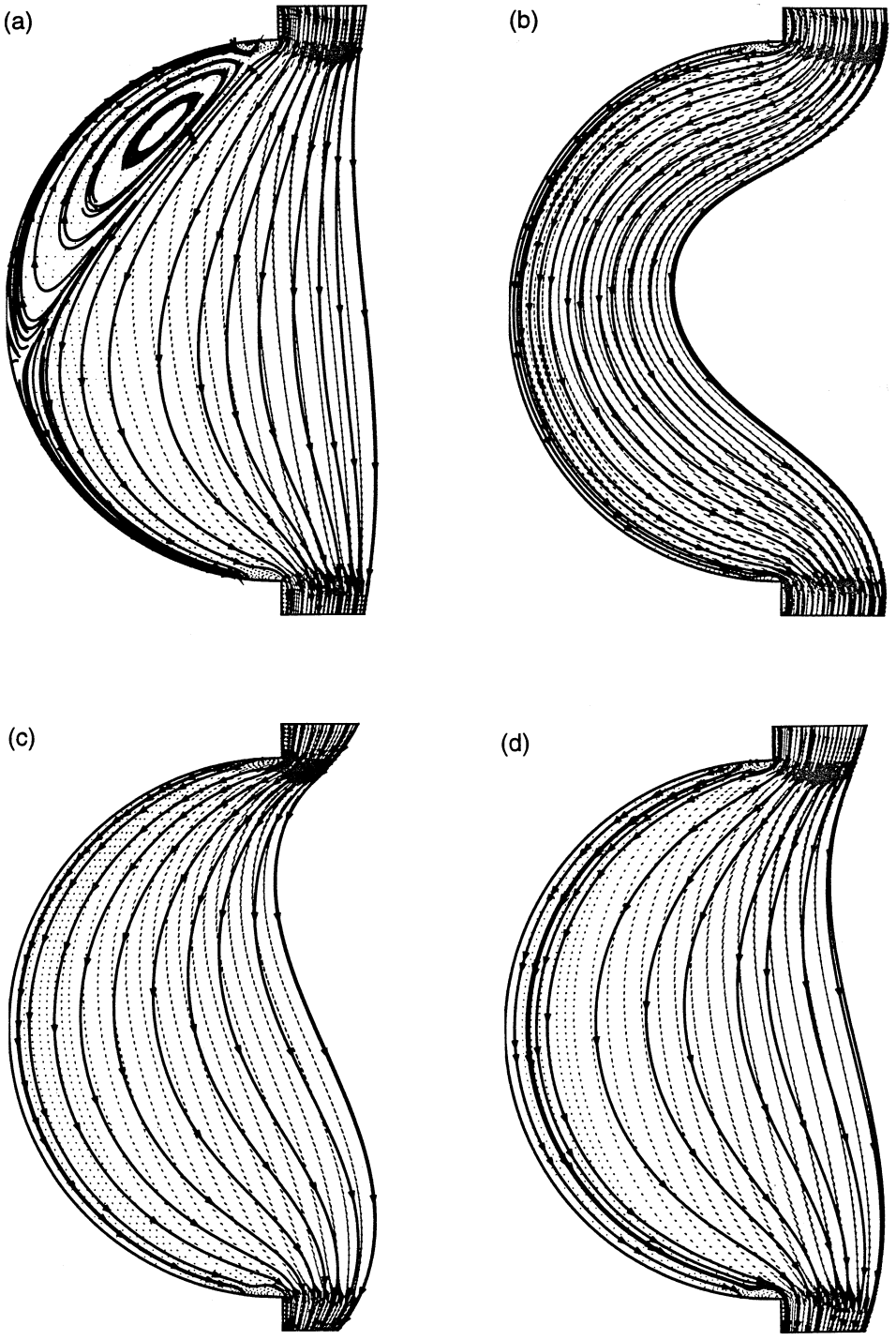

FIG. 14. Calculated streamlines of hypothetical numerical experiments around the flow conditions of the run of Fig. 10b. (a) exp. 2C, (b) exp. 2C with $Ca = 1$, (c) exp. 2C with $\gamma = 0.4$, and (d) exp. 2C with $Re = 1.5$.

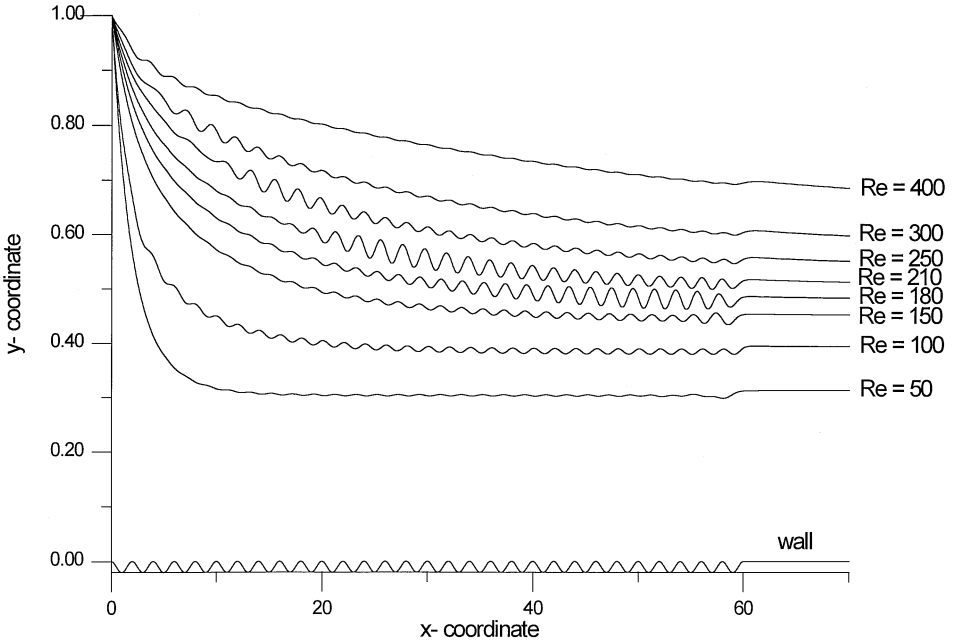

FIG. 15. Free surface profiles of a film flowing along an inclined wall with infinitesimal undulations, $a = 0.01$.

wavelength equals that of the wall in all cases tested. However, a *subharmonic* modulation seems to develop when approaching the resonance region from below. This is particularly evident for $Re = 100$ (Fig. 16a) and corresponds to wavelength twice that of the wall disturbance. At higher Reynolds numbers, free-surface waves develop blunt crests and a *superharmonic* modulation seems to appear for the highest wall amplitude (Fig. 17b, $Re = 300$). Both these phenomena disappear at the "resonant" region, which is dominated by the fundamental solution.

All results of the present work are for steady (developing or fully developed) flow. Stability analysis of the solutions, in particular around resonant *Re*, could be investigated next. It would be interesting if the present code were extended to incorporate spatially developing disturbances, thus enabling numerical experiments of convective instabilities.

5. CONCLUSIONS

In this work, a complete description of viscous flow along an inclined wall with infinitesimal and finite wall indentations is given in the whole range of laminar regime, taking into account all parameters that influence flow phenomena. At low Reynolds numbers, results of numerical experiments compare well with laboratory data at two different geometries of wall undulations.

Oscillations of the free surface increase, depending on the geometry of wall and the value of liquid surface tension. The wavelength of free surface oscillations is the same as the wavelength of the wall undulations and there is always a phase shift, due to the action of inertial and capillary forces. Velocity distributions at the free surface exhibit extreme values at points, where the size of the cross section between free surface and wall is also extreme. Correspondingly, pressure distributions along the free surface exhibit extreme values in the region of extreme values of the vertical component of free surface velocity.

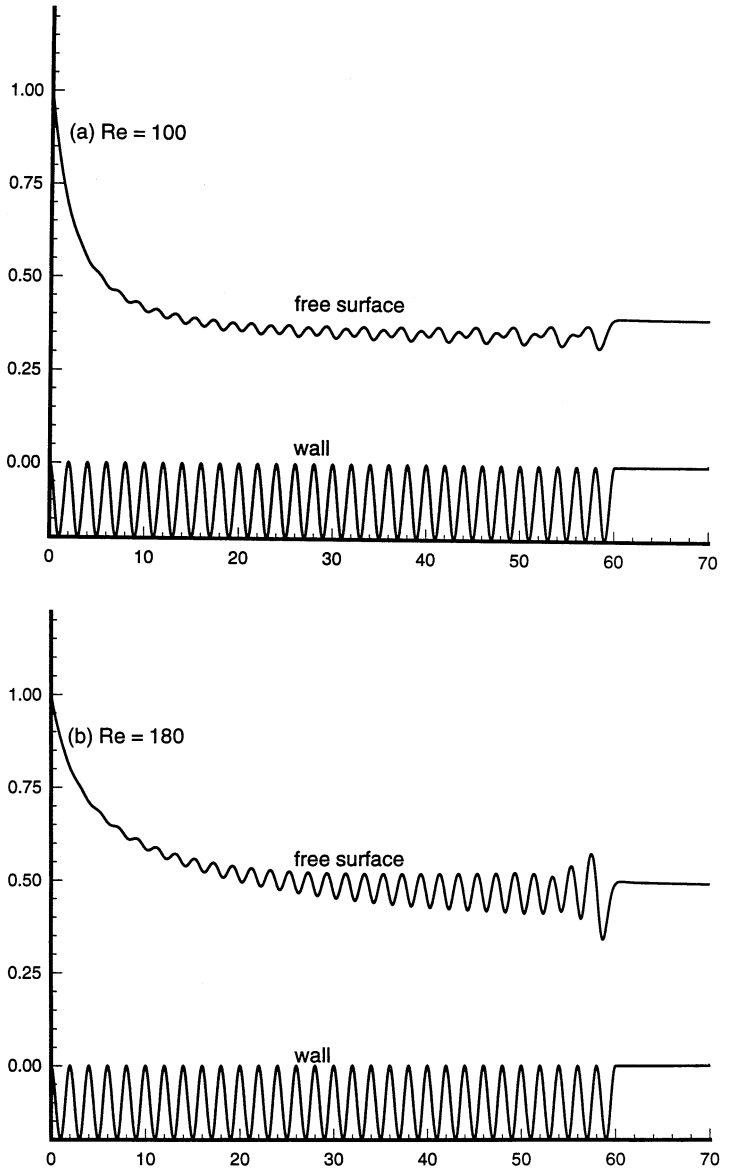

FIG. 16. Free surface profiles of a film flowing along an inclined wall with finite undulations, $a = 0.1$, (a) $Re = 100$, (b) $Re = 180$.

Among the dimensionless parameters of the flow, free surface shape is mainly influenced by the capillary number, its phase shift relative to the wall undulations by the Reynolds number, and film thickness by the dimensionless Nusselt film thickness. The distribution of shear stress and vorticity along the wall change sign at points of flow reversal.

Wall/free surface resonance is computed to occur at *Re* around 200 for short wall indentations and its non-linear behavior is investigated. Amplification factor decreases with wall amplitude. Subharmonic and superharmonic modulations are observed when approaching resonant *Re* from below and above, respectively.

All numerical experiments of this work have been designed with the same concept as actual laboratory experiments, using the free outflow boundary condition that enables the

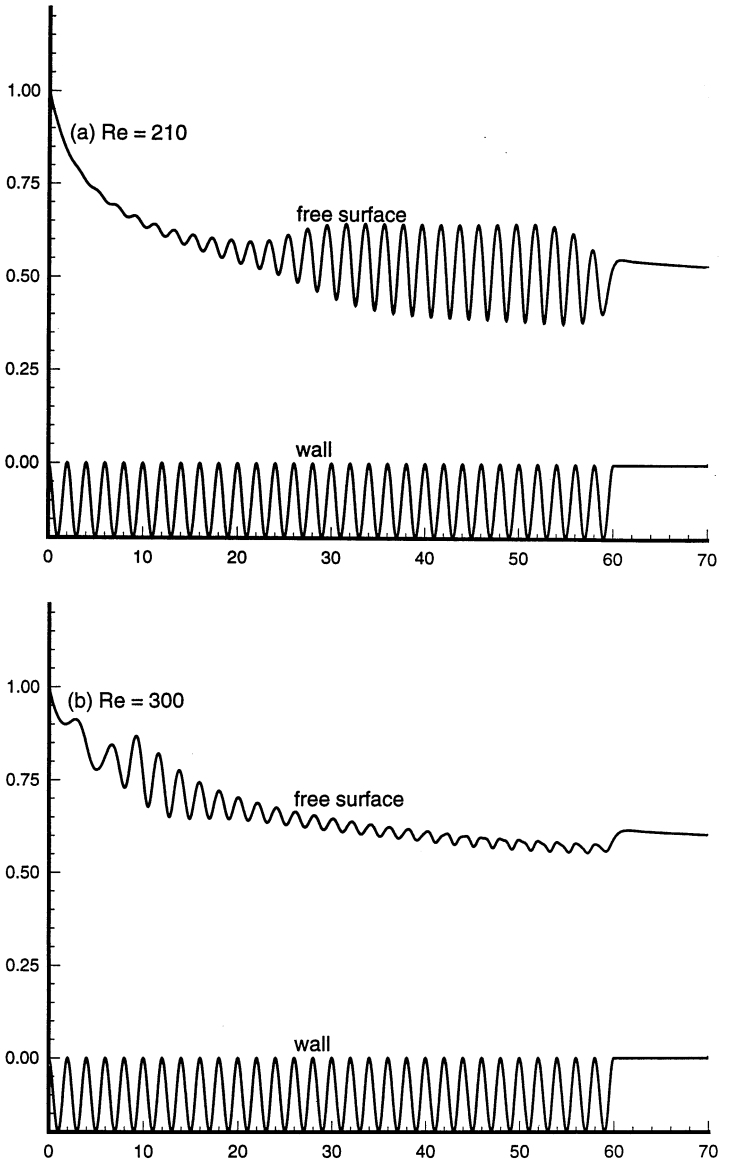

FIG. 17. Free surface profiles of a film flowing along an inclined wall with finite undulations, $a = 0.1$, (a) $Re = 210$, (b) $Re = 300$.

numerical analyst to construct a real computational domain. This is contrasted with traditional approaches to this flow problem involving the use of periodic boundary conditions at the in- and outflow of a computational domain of one period of oscillations, thus failing to provide information as to where the flow becomes fully developed and how the flow disturbance developes at high Reynolds numbers in the whole domain. The results are presently limited to steady state, which seems a useful first step in the analysis of this flow. The extent to which the steady state solution is a realistic approximation is not yet known experimentally. Stability analysis to the steady flow is a natural extension of the present work and will be considered next.

ACKNOWLEDGMENTS

We thank Dr.-Ing. T. Chatzikonstantinou and Dipl.-Math. T. Georgiou of Arithmotechniki Ltd. and Professor D. Diamantides of the Democritus University of Thrace for the permission to run our programs on their computing facilities. In the early part of this work, N.A.M. was financially supported by research Program 243 (ΕΠΕΤΠ) of the Hellenic Institute of Research and Technology directed by Professor N. S. Vlachos of the University of Thessaly.

REFERENCES

1. J. M. De Santos, T. R. Melli, and R. L. Scriven, Mechanics of gas–liquid flow in packed-bed contactors, *Ann. Rev. Fluid Mech.* **23**, 233 (1991).
2. S. Shetty and R. L. Cerro, Flow of a thin film over a periodic surface, *Int. J. Multiphase Flow* **19**(6), 1013 (1993).
3. V. Bontozoglou and G. Papapolymerou, Laminar film flow down a wavy incline, *Int. J. Multiphase Flow* **20**(1), 69 (1997).
4. C. Pozrikidis, The flow of a liquid film along a periodic wall, *J. Fluid Mech.* **188**, 275 (1988).
5. L. Zhao and R. L. Cerro, Experimental characterization of viscous film flows over complex surfaces, *Int. J. Multiphase Flow* **18**(4), 495 (1992).
6. C. Y. Wang, Liquid film flowing slowly down a wavy incline, *AIChE J.* **27**, 207 (1981).
7. C. G. Dassori, J. A. Deiber, and A. E. Cassano, Slow two-phase flow through a sinusoidal channel, *Int. J. Multiphase Flow* **10**, 181 (1984).
8. Y. Y. Trifonov, Viscous liquid film flows over a periodic surface, *Int. J. Multiphase Flow* **24**, 1139 (1998).
9. N. Malamataris and T. C. Papanastasiou, Unsteady free surface flows on truncated domains, *Ind. Eng. Chem. Res.* **30**, 2211 (1991).
10. N. Malamataris, *Computer-Aided Analysis of Flows on Moving and Unbounded Domains: Phase-Change Fronts and Liquid Leveling*, Ph.D. thesis, University of Michigan, Ann Arbor, MI, 1991.
11. T. C. Papanastasiou, N. Malamataris, and K. Ellwood, A new outflow boundary condition, *Int. J. Numer. Methods Fluids* **14**, 587 (1992).
12. R. L. Sani and P. M. Gresho, Résumé and remarks on the open boundary condition minisymposium, *Int. J. Numer. Methods Fluids* **18**, 983 (1994).
13. P. M. Gresho and R. L. Sani, *Incompressible Flow and the Finite Element Method* (Wiley, New York, 1998).
14. J. C. Heinrich and C. A. Vionnet, On boundary conditions for unbounded flows, *Comm. Numer. Methods Eng.* **11**, 179 (1995).
15. D. F. Griffiths, The “no boundary condition” outflow boundary condition, *Int. J. Numer. Methods Fluids* **24**, 393 (1997).
16. M. Renardy, Imposing “no” boundary condition at outflow: Why does it work?, *Int. J. Numer. Methods Fluids* **24**, 413 (1997).
17. R. Peyret and T. D. Taylor, *Computational Methods for Fluid Flow* (Springer-Verlag, New York, 1983).
18. P. Hood, Frontal solution program for unsymmetric matrices, *Int. J. Numer. Methods Eng.* **10**, 379 (1974).
19. S. F. Kistler and R. L. Scriven, Coating flow theory by finite element and asymptotic analysis of the Navier–Stokes system, in *Finite Element Flow Analysis*, edited by T. Kawai (Univ. of Tokyo Press, Tokyo, 1982).
20. K. N. Christodoulou and R. L. Scriven, Discretization of free surface flows and other moving boundary problems, *J. Comput. Phys.* **50**, 39 (1992).
21. R. C. J. Hunt, J. C. Abell, A. J. Peterka, and H. Woo, Kinematical studies of the flow around free- or suface-mounted obstacles; applying topology to flow visualization, *J. Fluid Mech.* **86**, 179 (1978).
22. V. P. Fragos, S. P. Psychoudaki, and N. A. Malamataris, Computer-aided analysis of flow past a surface-mounted obstacle, *Int. J. Numer. Meth. Fluids* **25**, 495 (1997).